2017

Superior Li storage anode based on novel Fe-Sn-P alloy prepared by electroplating

Xiao Zheng
China Jiliang University

Peng Zhang
China Jiliang University

Liang Wang
China Jiliang University

Shan Tao
China Jiliang University

Yunxiao Wang
University of Wollongong, yunxiao@uow.edu.au

See next page for additional authors

Publication Details

Zheng, X., Zhang, P., Wang, L., Tao, S., Wang, Y., Huang, L., Sun, S. & Li, J. (2017). Superior Li storage anode based on novel Fe-Sn-P alloy prepared by electroplating. Electrochimica Acta, 247 314-320.

Superior Li storage anode based on novel Fe-Sn-P alloy prepared by electroplating

Abstract

Novel ternary Fe-Sn-P alloys prepared by simple single-step electrodeposition are investigated as promising anodes for Li-ion batteries. The Fe 51 Sn 38 P 11 electrode, in particular, shows outstanding Li-storage properties, with initial specific discharge/charge capacities of 857.8 and 655 mA h g ¿1 , respectively. The reversible capacity remains stable at 427 mA h g ¿1 , even after 90 cycles, corresponding to a coulombic efficiency of 96% and a capacity retention of 65%. The cauliflower-like morphology of the above anode is well preserved after 90 cycles, suggesting that this alloy could significantly mitigate the electrode volume expansion by exerting a positive multiphase synergistic effect. The superior electrochemical performance of the ternary Fe-Sn-P alloys confirmed its potential as an alternative Li-ion storage anode; the large-scale suitability of the developed electroplating method provides an additional advantage.

Disciplines

Engineering | Physical Sciences and Mathematics

Publication Details

Zheng, X., Zhang, P., Wang, L., Tao, S., Wang, Y., Huang, L., Sun, S. & Li, J. (2017). Superior Li storage anode based on novel Fe-Sn-P alloy prepared by electroplating. Electrochimica Acta, 247 314-320.

Authors

Xiao Zheng, Peng Zhang, Liang Wang, Shan Tao, Yunxiao Wang, Ling Huang, Jun-Tao Li, and Shi-Gang Sun

Superior Li storage anode based on novel Fe-Sn-P alloy prepared by electroplating

Xiao-Mei Zheng[a*], Peng-Yue Zhang[a*], Liang-ke Wang[a], Shan Tao[a], Yun-Xiao Wang[c], Ling Huang[b], Jun-Tao Li[b], Shi-Gang Sun[b]

a. China Jiliang University, Magnetism Key Lab Zhejiang Province, Hangzhou, 310018, China.

b. Department of chemistry, College of Chemistry and Chemical Engineering, State key laboratory of physical chemistry of solid surfaces, Xiamen University, Xiamen, 361005, China

c. Institute for Superconducting & Electronic Materials (ISEM) Innovation Campus, University of Wollongong, Wollongong, NSW, 2519 (Australia)

[*]Corresponding author. Tel.: +86-571-87676238; fax: +86-571-87676238

E-mail: Zheng_xiaomei@cjlu.edu.cn or Zhang_pengyue@cjlu.edu.cn

Abstract: Novel ternary Fe-Sn-P alloys prepared by simple single-step electrodeposition are investigated as promising anodes for Li-ion batteries. The $Fe_{51}Sn_{38}P_{11}$ electrode, in particular, shows outstanding Li-storage properties, with initial specific discharge/charge capacities of 857.8 and 655 mA h g^{-1}, respectively. The reversible capacity remains stable at 427 mA h g^{-1}, even after 90 cycles, corresponding to a coulombic efficiency of 96% and a capacity retention of 65%. The cauliflower-like morphology of the above anode is well preserved after 90 cycles, suggesting that this alloy could significantly mitigate the electrode volume expansion by exerting a positive multiphase synergistic effect. The superior electrochemical performance of the ternary Fe-Sn-P alloys confirmed its potential as an alternative Li-ion storage anode; the large-scale suitability of the developed electroplating method provides an additional advantage.

Keywords: metal phosphides; tin-based anode; lithium-ion battery; electrodeposition; negative electrode

1. Introduction

Rechargeable Li-ion batteries (LIBs), as well as supercapacitors, exhibit high power density, high safety, and long lifetimes, thereby playing an important role in our daily life because they are widely used in electronic devices, implantable medical devices, smart grid systems, and vehicles [1-5]. However, the accessible capacities of Li-ion batteries still cannot meet the fast-growing energy demand of newly emerging applications such as electric vehicles. Therefore, the development of anode materials with high capacities and superior cyclabilities as alternatives to graphite materials (372 mA h g^{-1}) for Li-ion batteries has become increasingly important. Among the various potential anode materials, phosphorus has recently attracted much attention because of its high theoretical discharge capacity (2596 mA h g^{-1}), unique puckered layer structure, and low Li intercalation potential (0.02–0.2 V) [6-8]. The puckered layer structure with a low stacking density of 30% can release structural strain and enable fast diffusion of Li^+, thus enhancing the electrochemical cycling stability. Because the electronic conductivity of P is rather poor, extensive research has been conducted on transition metal phosphides (MPs) that can effectively improve the overall electronic conductivity of the electrode, affording enhanced Li-storage properties [9-11]. However, the commercial application of MP anodes is hindered by their large volume changes upon Li insertion and extraction that result in particle pulverization and rapid capacity fading [12]. So far, various binary MPs such as MnP_4, FeP_x, CoP_3, Cu_3P, NiP_2, $SnP_{0.94}$, and Sn_4P_3 have been fabricated via high-temperature solid-state synthesis, ball milling, solution-phase techniques, and other traditional time-consuming and high-cost stepwise methods [7, 9, 12-18], which often require extreme operating conditions incompatible with practical applications.

In recent years, ternary metal phosphides (e.g., Sb-Co-P, Fe-Sb-P, and Sn-Ni-P) and even a

quaternary Fe-Sn-Sb-P system have been explored as alternatives to binary MPs [19-22]. The introduction of inactive elements (Fe/Ni/Co) can not only effectively alleviate the mechanical stress induced by active phase (Sn/Sb/P) volume changes, but also enhance electron transfer and dynamic/mechanical strength. More importantly, these ternary/quaternary phosphides can be prepared via single-step electroplating, which is cost-effective and easy to scale-up, allowing facile film deposition onto substrates. In addition, the electroplating technique is flexible and adjustable, allowing one to control the composition, morphology, and thickness of the produced thin films via a simple variation of the current density and plating time.

Herein, we report a novel multiphase Fe-Sn-P composite via a facile single-step electroplating method. Five ternary Fe-Sn-P alloys of different compositions were electrochemically deposited on copper foil substrates; the optimal performance was observed for $Fe_{51}Sn_{38}P_{11}$. The Fe-Sn-P alloys were used to prepare a binder-free LIB anode, delivering high capacity and superior cycling performance. Thus, these alloys hold great promise as a superior Li storage anode.

2. Experimental section

2.1 Linear sweep voltammetry (LSV) characterization

All electrochemical analyses were conducted using an electrochemical workstation (CHI660C, Chenhua Instruments, China) and a three-electrode setup. A Pt sheet (exposed area = 2 cm^2) and a glassy carbon electrode (diameter = 0.5 mm) were employed as the counter and working electrodes, respectively, and the potential applied between them was regulated using a reference saturated calomel electrode (SCE).

2.2 Fabrication of Fe-Sn-P multiphase composite electrodes

Fe-Sn-P alloys were galvanostatically fabricated at room temperature using a potentiostat; the composition, content, and function of each reagent are listed in **Table 1**. The pH was adjusted to

1.5 by utilizing 1 M hydrochloric acid. All chemicals were of reagent grade and were dissolved in distilled water. A Pt foil with an area of 4 cm^2 was used as a counter electrode, with the SCE used as a reference. Fe-Sn-P electrodes were deposited on Cu foil circles (diameter = 1.6 cm, exposed surface area = 2.0 cm^2) at an applied current density of 8.85–44.25 A dm^{-2} for 2 min.

2.3 Material characterization

The crystal structures of the deposited materials were investigated by powder X-ray diffraction (XRD; Philips X'pert Pro Super X-ray diffractometer, Netherlands, Cu K_α radiation, λ = 1.5408 Å) at a scan rate of 2° min^{-1}. The morphology and elemental composition of the electrodeposited films were determined by field emission scanning electron microscopy (SEM, Hitachi S-4800) coupled with energy dispersive X-ray spectroscopy (EDX). The binding energies of Fe, Sn, and P in as-prepared Fe-Sn-P alloys were determined by X-ray photoelectron spectroscopy (XPS, Quantum 2000 spectrometer, USA)

2.4 Electrochemical performance characterization

As-deposited Fe-Sn-P electrodes were heated to 80 °C under vacuum for 12 h, and their electrochemical behavior was characterized using a two-electrode cell; a lithium foil was used as a reference/counter electrode. All CR2025 coin cells were assembled in an Ar-filled glove box (with H_2O and O_2 levels being less than 2 ppm). The electrolyte corresponded to a 1.0 M solution of $LiPF_6$ in a mixture of diethyl carbonate (DEC), dimethyl carbonate (DMC), and ethylene carbonate (EC) (DEC:DMC:EC = 1:1:1 v/v/v) containing 2 wt% of vinylene carbonate (VC, provided by Guangzhou Tinci Materials Technology Co., Ltd., China). A Celgard 2400 polypropylene membrane was used as a separator.

Galvanostatic charge-discharge tests of Li/Fe-Sn-P half-cells were performed using a LAND-V34 (Wuhan, China) battery tester at a rate of 100 mA g^{-1} in a fixed voltage range of

1.5–0.02 V at room temperature. The cycled electrodes were dismantled in the glove box, washed with DMC and acetone for three times, and reserved in a special box sealed with epoxy resin glue prior to SEM measurements.

3. Results and discussion

Fe-P and Fe-Sn-P films deposited on the Cu substrate were characterized by cathodic LSV, which was performed in cathodic direction from –0.6 to –1.15 V at room temperature and a scan rate of 5 mV s^{-1} (**Fig. 1a**). Curve 1 (red line in **Fig. 1a**) was recorded in a solution of 0.6 M H_3BO_3, 1.0 M NH_4Cl, 0.5 M $NaH_2PO_2 \cdot H_2O$, and 0.05 M $FeCl_2 \cdot 4H_2O$. A rapid increase in current density was observed between –1.09 and –1.5 V (vs. SCE), associated with Fe-P electrodeposition and simultaneous evolution of hydrogen, in agreement with a previous study [20]. Significant changes were observed upon incorporation of Sn^{2+} ions into the Fe-P system, such as the appearance of a new reduction peak at around –0.65 V (curve 2, black line). This peak was attributed to the deposition of Sn, as confirmed by SEM and EDX (inset) measurements (**Fig. 1b**). Ternary alloy deposition occurred at potentials more negative than –1.0 V. Under these conditions, curve 2 was observed to have a higher current density than curve 1 because of the electrodeposition of Sn on the Cu substrate. To confirm Sn deposition at –0.65 V, a thin film was deposited on the Cu substrate from the same solution at –0.65 V for 10 min. The corresponding SEM image in **Fig. 1b** shows numerous stripes on the thin film surface, without any other special features. As illustrated in the inset of **Fig. 1b,** EDX results demonstrate that the deposit obtained at –0.65 V consists of Sn, and the weak intensity of the Sn peak indicates the low amount of this metal. The peak of Cu was attributed to the Cu matrix. No peaks of other elements were observed, implying that pure Sn was deposited at around –0.65 V. When cathodic scanning was carried out at -1.5 V, a ternary Fe-Sn-P alloy was obtained. As shown in **Fig. 1c**,

the SEM image reveals that the as-deposited Fe-Sn-P (denoted as $Fe_{51}Sn_{38}P_{11}$) exhibits uniform and compact packing without holes or cracks. It features cauliflower-like aggregates composed of nanoparticles, most of which are spherical and exhibit sizes between 50 and 1.5 μm. This cauliflower-like morphology provides more active sites for electrochemical reactions due to its large specific surface area, as compared to those of planar or spherical particles. This morphology effectively alleviates the volume expansion induced by repeated Li^+ insertion and extraction. Moreover, the elemental mappings of element Fe, Sn, and P shown in **Figs. 1d-f** confirm that these elements are homogenously dispersed in the composite without any impurity.

The reactions on the Cu surface can be expressed as follows [23]:

$$H_2PO_2^- + 2H^+ + e^- \rightarrow P + 2H_2O \quad (1)$$

$$Fe^{2+} + 2e^- \rightarrow Fe \quad (2)$$

$$Sn^{2+} + 2e^- \rightarrow Sn \quad (3)$$

$$2H^+ + 2e^- \rightarrow H_2\uparrow \quad (4)$$

Generally, the deposit composition is significantly affected by current densities. Therefore, five Fe-Sn-P alloys of different compositions ($Fe_{51}Sn_{38}P_{11}$, $Fe_{58}Sn_{30}P_{12}$, $Fe_{70}Sn_{16}P_{14}$, $Fe_{75}Sn_{10}P_{15}$, and $Fe_{73}Sn_{13}P_{14}$) were electrochemically deposited from the same electrolyte at various current densities (**Table 2** and **Fig. 2a**). The contents of Fe and P in these alloys increased with increasing current density, whereas that of Sn concomitantly decreased. The crystalline phases of the as-deposited Fe-Sn-P alloys were further probed by XRD (**Fig. 2b**). The peaks of Fe_3Sn (2θ = 43.2°; JCPDS No. 03-065-3524), Sn (2θ = 30.5°, 32.0°, and 45.0°; JCPDS No. 00-001-0926), and SnP (2θ = 86.0°; JCPDS No. 00-021-1230) were clearly identified for $Fe_{51}Sn_{38}P_{11}$ deposited at 8.85 A dm^{-2}; no other peaks were detected except for those of the Cu substrate (2θ = 50.4°, 74.0°, and 89.9°). For $Fe_{58}Sn_{30}P_{12}$, the peak of SnP was not observed, and the intensities of the

Fe_3Sn and Sn peaks were weaker than those of $Fe_{51}Sn_{38}P_{11}$. When the current density was increased to 26.5–44.25 A dm^{-2}, a broad peak was observed at 40–45°, indicating that the Fe-Sn-P alloys deposited under these conditions were amorphous due to their high P content (as determined by EDX) [24, 25]. Besides, a very weak peak of Fe_3Sn was observed at 2θ = 43.2° (JCPDS No. 03-065-3524), indicating that the content of this phase in the above alloys was very low. Thus, increasing current density induced a crystalline-to-amorphous structural transition, allowing the preparation of two multiphase and three amorphous Fe-Sn-P electrodes at low and high current densities, respectively. When a Fe-Sn-P multi-phase composite electrode was used an LIB anode, the inactive Fe component therein maintained good electronic conduction and could withstand the mechanical stress induced by the alloying/de-alloying of P and Sn with Li^+ because the electrode exhibits excellent mechanical strength, chemical inertness, and electrical conductivity. Furthermore, Fe played an important barrier role, preventing the agglomeration of active materials (Sn and P) and enhancing the cycling performance during the charge/discharge processes [26-29]. Thus, such multiphase Fe-Sn-P alloy electrodes were expected to exhibit better cycling performance than their amorphous counterparts.

The chemical composition of the Fe-Sn-P alloy deposited at 8.85 A dm^{-2} was examined by EDX. **Figure 3a** presents the EDX spectrum of $Fe_{51}Sn_{38}P_{11}$, revealing the presence of Fe, Sn, and P only, with the exception of substrate-originated Cu. The weaker intensities of Sn and P peaks compared to that of the Fe peak indicate the lower contents of these elements in the alloy. The presence of $Fe_{51}Sn_{38}P_{11}$ was further confirmed by XPS, with the corresponding spectrum (**Fig. 3b**) showing major peaks at ~130 (P 2p), 500 (Sn 3d), and 724 (Fe 2p) eV, confirming the simultaneous presence of Fe, P, and Sn, in agreement with the results of EDX analysis.

To further investigate the effects of composition and structure on the electrochemical

performance, three sample Fe-Sn-P alloys prepared at 8.85, 26.5, and 44.25 A dm^{-2} were investigated as anodes in half-cell LIBs. Their Li storage behavior is shown in **Fig. 4**. Using the multielectron reactions(Sn + 4.4 Li ⇋ $Li_{4.4}Sn$; P + 3 Li ⇋ Li_3P) [30], the theoretical capacities of $Fe_{51}Sn_{38}P_{11}$, $Fe_{70}Sn_{16}P_{14}$, and $Fe_{73}Sn_{13}P_{14}$ were calculated to be 698.3, 481.3, and 439.4 mA h g^{-1}, respectively. The battery with the $Fe_{51}Sn_{38}P_{11}$ anode is expected to deliver the best electrochemical performance. As shown in **Fig. 4a**, **b**, and **c**, $Fe_{51}Sn_{38}P_{11}$, $Fe_{70}Sn_{16}P_{14}$, and $Fe_{73}Sn_{13}P_{14}$ displayed the initial discharge capacities of 857.8, 609, and 612.6 mA h g^{-1}, respectively, at a current density of 100 mA g^{-1}. Using the corresponding charge capacities of 655, 476, and 474 mA h g^{-1}, the initial coulombic efficiencies were estimated as 76%, 78%, and 77%, respectively. According to previous studies [31, 32], low initial coulombic efficiencies are caused by the electrolyte decomposition (DMC and DEC), irreversible reaction of oxide impurities, and formation of a solid electrolyte interface (SEI) layer on the electrode surface. Importantly, the greatly increased coulombic efficiency (>96%) observed from the second cycle onwards demonstrates that such irreversible reactions were significantly suppressed by SEI layer formation on the electrode surfaces of these three samples. After 90 cycles, the capacities of the $Fe_{70}Sn_{16}P_{14}$ and $Fe_{73}Sn_{13}P_{14}$ anodes significantly decreased. Conversely, $Fe_{51}Sn_{38}P_{11}$ exhibited the highest discharge and charge capacities (857.8 and 427 mA h g^{-1}, respectively) and retained the best cycling performance, which was attributed to its optimized composition. In Fe-Sn-P alloys, lithium intercalation is enabled by the presence of both Sn and P, which react with Li^+ at 0.05–0.4 and 0.02–0.2 V (vs. Li^+/Li), respectively. When Li^+ reacts with Sn at a higher voltage, P and Fe act as an inactive matrix to alleviate the volume change of Sn. Similarly, the insertion of Li ions into P to form Li_xP at a lower voltage is buffered by the Li-Sn alloy. Moreover, the introduced inactive Fe-containing intermetallic compound (Fe_3Sn) increases the electronic conductivity and

acts as a buffer matrix, thereby improving the cell cyclability. The above XRD analysis results show that even though $Fe_{51}Sn_{38}P_{11}$ is crystalline and $Fe_{70}Sn_{16}P_{14}$ and $Fe_{73}Sn_{13}P_{14}$ are amorphous, all three samples exhibit a similar cycling trend with different capacities, indicating that the cycling performance of Fe-Sn-P alloy electrodes depends on the phase composition but not on the crystal structure. The high discharge/charge capacity of $Fe_{51}Sn_{38}P_{11}$ was ascribed to its higher Sn content than that of $Fe_{70}Sn_{16}P_{14}$ and $Fe_{73}Sn_{13}P_{14}$, as determined by EDX analysis. Since pure Sn was not detected by XRD, the Sn contained in this alloy could react with lithium to deliver lithium storage capacity. Thus, $Fe_{51}Sn_{38}P_{11}$, with the highest Sn content, showed better electrochemical performance than the other two Fe-Sn-P alloy electrodes. Notably, the electrochemical performance of the developed FeSnP anode was superior to those of the Sb-Co-P and Fe-Sb-P composite electrodes reported by our group previously [19, 22].

Figure 4d depicts the discharge-charge voltage profiles of the $Fe_{51}Sn_{38}P_{11}$ composite electrode for the 1st, 2nd, 30th, 60th, and 90th cycles. The sloping region at 1.5–0.8 V (vs. Li^+/Li) in the initial discharge curve was assigned to the suppression of the irreversible reaction with the electrolyte and the presence of possible oxide impurities on the anode surface. These irreversible reactions accounted for the large irreversible capacity that is often unavoidable in electrochemical cycling. Three obvious discharge curve plateaus at 0.7, 0.54, and 0.45 V were attributed to Sn alloying with Li^+ to form Li_xSn ($x < 2.33$) [33]. Reactions occurring below 0.2 V were ascribed to the formation of Li_3P [34]. The sloping region observed during charging at 0.3–1.1 V was assigned to Li_xSn and Li_xP delithiation.

Figure 5a shows the SEM image of the $Fe_{51}Sn_{38}P_{11}$ electrode after complete delithiation after 90 cycles, revealing that the structural integrity of the particles is well preserved despite their slightly increased size, with no evident sign of pulverization. No obvious SEI formation could be

detected on the anode surface, indicating that the produced SEI film was transparent and very thin, achieving suitable coulombic efficiency, in agreement with the results shown in **Fig. 4**. Similar to the as-prepared sample (**Fig. 1c**), the EDX mappings after 90 cycles shown in **Figs. 5b-d** did not show any elemental agglomeration, in which Fe, Sn, and P are well-dispersed over the sample. It also indicates that the prepared structures can be maintained over repeated cycling process, which is consistent with the good cycling stability of $Fe_{51}Sn_{38}P_{11}$ (**Fig. 4a**).

Thus, the electrochemical reaction between $Fe_{51}Sn_{38}P_{11}$ and Li^+ occurred in a reversible and stable manner, with the capacity degradation caused by electric contact loss effectively suppressed. The excellent capacity storage and cycling performance was ascribed to the unique cauliflower-like morphology and multiphase composition of the $Fe_{51}Sn_{38}P_{11}$ composite electrode, which provides elastic accommodation to restrain volume changes and electrode pulverization during discharge/charge processes.

4. Conclusions

In summary, we have prepared novel ternary Fe-Sn-P alloy electrodes of different compositions via single-step electroplating and examined their electrochemical performances as LIB anodes. The results revealed that the multiphase $Fe_{51}Sn_{38}P_{11}$ electrode can exhibit outstanding cycling stability and high specific capacity, showing initial discharge and charge capacities of 857.8 and 655 mA h g^{-1}, respectively. The corresponding charge capacity is sustained at 427 mA h g^{-1} over 90 cycles at a high coulombic efficiency of 96%, with the charge capacity retention equaling 65%. The high Li-storage capacity and superior cyclability of this ternary electrode were attributed to its cauliflower-like structure and multi-phase composition (Sn, Fe_3Sn, and SnP phases). Thus, this study demonstrates that it is feasible to prepare novel binder- and conductive agent-free P-based electrodes for potential application in LIBs by electroplating.

Acknowledgements

This work was supported by the National Natural Science Foundation of China (Nos. 51401199, 51401180, 51301158, and 51371163), the National Key Research and Development Program of China (No. 2016YFB0100202) and Provincial Natural Science Foundation (LR15E010001 and LQ15E010005).

References

[1] M. Armand, J.M. Tarascon, Building better batteries, Nature 451(7179) (2008) 652-657.

[2] B. Kang, G. Ceder, Battery materials for ultrafast charging and discharging, Nature 458(7235) (2009) 190-193.

[3] K.S. Kang, Y.S. Meng, J. Breger, C.P. Grey, G. Ceder, Electrodes with high power and high capacity for rechargeable lithium batteries, Science 311(5763) (2006) 977-980.

[4] Y. Yan, P. Gu, S. Zheng, M. Zheng, H. Pang, H. Xue, Facile synthesis of an accordion-like Ni-MOF superstructure for high-performance flexible supercapacitors, Journal of Materials Chemistry A 4(48) (2016) 19078-19085.

[5] Y. Yan, B. Li, W. Guo, H. Pang, H. Xue, Vanadium based materials as electrode materials for high performance supercapacitors, Journal of Power Sources 329 (2016) 148-169.

[6] C.-M. Park, H.-J. Sohn, Novel antimony/aluminum/carbon nanocomposite for high-performance rechargeable lithium batteries, Chemistry of Materials 20(9) (2008) 3169-3173.

[7] D.C.S. Souza, V. Pralong, A.J. Jacobson, L.F. Nazar, A reversible solid-state crystalline transformation in a metal phosphide induced by redox chemistry, Science 296(5575) (2002)

2012-2015.

[8] C.-M. Park, H.-J. Sohn, Black phosphorus and its composite for lithium rechargeable batteries, Advanced Materials 19(18) (2007) 2465-2468.

[9] Y. Lu, T. Wang, X. Li, G. Zhang, H. Xue, H. Pang, Synthetic methods and electrochemical applications for transition metal phosphide nanomaterials, RSC Advances 6(90) (2016) 87188-87212.

[10] Y. Shi, B. Zhang, Recent advances in transition metal phosphide nanomaterials: synthesis and applications in hydrogen evolution reaction, Chemical Society reviews 45(6) (2016) 1529-1541.

[11] J.M. Cameron, R.W. Hughes, Y. Zhao, D.H. Gregory, Ternary and higher pnictides; prospects for new materials and applications, Chemical Society reviews 40(7) (2011) 4099-4118.

[12] Y. Kim, H. Hwang, C.S. Yoon, M.G. Kim, J. Cho, Reversible lithium intercalation in teardrop-shaped ultrafine $SnP_{0.94}$ particles: an anode material for lithium-ion batteries, Advanced Materials 19(1) (2007) 92-96.

[13] V. Pralong, D.C.S. Souza, K.T. Leung, L.F. Nazar, Reversible lithium uptake by CoP_3 at low potential: role of the anion, Electrochemistry Communications 4(6) (2002) 516-520.

[14] S. Boyanov, D. Zitoun, M. Menetrier, J.C. Jumas, M. Womes, L. Monconduit, Comparison of the electrochemical lithiation/delithiation mechanisms of FeP_x (x=1, 2, 4) based electrodes in Li-ion batteries, Journal of Physical Chemistry C 113(51) (2009) 21441-21452.

[15] J.W. Hall, N. Membreno, J. Wu, H. Celio, R.A. Jones, K.J. Stevenson, Low-temperature synthesis of amorphous FeP_2 and its use as anodes for Li ion batteries, Journal of the American Chemical Society 134(12) (2012) 5532-5535.

[16] M. Fan, Y. Chen, Y. Xie, T. Yang, X. Shen, N. Xu, H. Yu, C. Yan, Half-cell and full-cell

applications of highly stable and binder-free sodium ion batteries based on Cu_3P nanowire anodes, Advanced Functional Materials 26(28) (2016) 5019-5027.

[17] S. Liu, J. Feng, X. Bian, J. Liu, H. Xu, Electroless deposition of Ni_3P-Ni arrays on 3-D nickel foam as a high performance anode for lithium-ion batteries, RSC Advances 5(75) (2015) 60870-60875.

[18] S. Liu, H. Zhang, L. Xu, L. Ma, X. Chen, Solvothermal preparation of tin phosphide as a long-life anode for advanced lithium and sodium ion batteries, Journal of Power Sources 304 (2016) 346-353.

[19] X.-M. Zheng, Y. Xiao, L. Huang, F.-S. Ke, Y. He, J.-T. Li, G.-Z. Wei, S.-G. Sun, Fabrication and electrochemical properties of novel ternary Sb-Co-P alloy electrodes for lithium-ion batteries, Electrochemistry Communications 11(9) (2009) 1803-1806.

[20] X.-M. Zheng, L. Huang, Y. Xiao, H. Su, G.-l. Xu, F. Fu, J.-T. Li, S.-G. Sun, A dicranopteris-like Fe-Sn-Sb-P alloy as a promising anode for lithium ion batteries, Chemical Communications 48(54) (2012) 6854-6856.

[21] Y.-X. Wang, L. Huang, Y.-Q. Chang, F.-S. Ke, J.-T. Li, S.-G. Sun, Fabrication and electrochemical properties of the Sn-Ni-P alloy rods array electrode for lithium-ion batteries, Electrochemistry Communications 12(9) (2010) 1226-1229.

[22] L. Huang, X.-M. Zheng, Y.-S. Wu, L.-J. Xue, F.-S. Ke, G.-Z. Wei, S.-G. Sun, Electrodeposition and lithium storage performance of novel three-dimensional porous Fe-Sb-P amorphous alloy electrode, Electrochemistry Communications 11(3) (2009) 585-588.

[23] K. Sridharan, K. Sheppard, Electrochemical characterization of Fe-Ni-P alloy electrodeposition, Journal of Applied Electrochemistry 27(10) (1997) 1198-1206.

[24] F. Wang, K. Itoh, T. Watanabe, Relationship between the crystallographic structure of

electrodeposited Fe-P alloy film and its thermal equilibrium phase diagram, Materials Transactions 44(1) (2003) 127-132.

[25] D.S. Xue, H.G. Shi, The fabrication and characteristic properties of amorphous $Fe_{1-x}P_x$ alloy nanowire arrays, Nanotechnology 15(12) (2004) 1752-1755.

[26] O. Mao, J.R. Dahn, Mechanically alloyed Sn-Fe(-C) powders as anode materials for Li-ion batteries - III. Sn_2Fe : $SnFe_3C$ active/inactive composites, Journal of the Electrochemical Society 146(2) (1999) 423-427.

[27] O. Mao, R.A. Dunlap, J.R. Dahn, Mechanically alloyed Sn-Fe(-C) powders as anode materials for Li-ion batteries - I. The Sn_2Fe-C system, Journal of the Electrochemical Society 146(2) (1999) 405-413.

[28] F. Xin, X. Wang, J. Bai, W. Wen, H. Tian, C. Wang, W. Han, A lithiation/delithiation mechanism of monodispersed MSn5 (M = Fe, Co and FeCo) nanospheres, Journal of Materials Chemistry A 3(13) (2015) 7170-7178.

[29] J.T. Yin, M. Wada, S. Tanase, T. Sakai, Nanocrystalline Ag-Fe-Sn anode materials for Li-ion batteries, Journal of the Electrochemical Society 151(4) (2004) A583-A589.

[30] X.-P. Gao, H.-X. Yang, Multi-electron reaction materials for high energy density batteries, Energy & Environmental Science 3(2) (2010) 174-189.

[31] J.-T. Li, J. Swiatowska, A. Seyeux, L. Huang, V. Maurice, S.-G. Sun, P. Marcus, XPS and ToF-SIMS study of Sn-Co alloy thin films as anode for lithium ion battery, Journal of Power Sources 195(24) (2010) 8251-8257.

[32] J.-T. Li, S.-R. Chen, X.-Y. Fan, L. Huang, S.-G. Sun, Studies of the interfacial properties of an electroplated Sn thin film electrode/electrolyte using in situ MFTIRS and EQCM, Langmuir 23(26) (2007) 13174-13180.

[33] X. Fan, P. Dou, A. Jiang, D. Ma, X. Xu, One-step electrochemical growth of a three-dimensional Sn-Ni@PEO nanotube array as a high performance lithium-ion battery anode, ACS Applied Materials & Interfaces 6(24) (2014) 22282-22288.

[34] S. Boyanov, J. Bernardi, F. Gillot, L. Dupont, M. Womes, J.M. Tarascon, L. Monconduit, M.L. Doublet, FeP: Another attractive anode for the Li-ion battery enlisting a reversible two-step insertion/conversion process, Chemistry of Materials 18(15) (2006) 3531-3538.

Table 1. Composition of the bath and electroplating conditions used for the preparation of Fe-Sn-P alloys.

Table 2. Chemical composition of Fe-Sn-P alloys deposited at different current density.

Bath composition	Concentration (M)	Function
$SnCl_2 \cdot 2H_2O$(stannous chloride)	0.03	Source of Sn
H_3BO_3(boric acid)	0.60	Buffer agent
NH_4Cl(ammonium chloride)	1.00	Complex agent
$NaH_2PO_2 \cdot H_2O$(sodium hypophosphite)	0.5	Source of P
$FeCl_2 \cdot 4H_2O$(ferrous chloride)	0.05	Source of Fe
Electro-deposition parameters	value	
Current density (A/dm^2)	8.85–44.25	
pH	1.5	
Temperature	Room temperature	
Plating time	2 min	

Table 1

Current density A/dm^2	8.85	17.7	26.5	35.40	44.25
	At%	At%	At%	At%	At%
Fe	50.8	58.2	70.2	75.0	73.0
Sn	38.1	30.3	16.1	10.3	13.2
P	11.1	11.5	13.7	14.7	13.8
Total %	100	100	100	100	100

Table 2

Figures and Figure Captions

Figure 1 (a) Linear sweep voltammetry (LSV) of Fe-P and Fe-Sn-P alloy deposition in different solutions.

(1) 0.6 MH_3BO_3, 1.0 M NH_4Cl, 0.5 M $NaH_2PO_2 \cdot H_2O$, and 0.05 M $FeCl_2 \cdot 4H_2O$;

(2) 0.03 M $SnCl_2 \cdot 6H_2O$, 0.6 MH_3BO_3, 1.0 M NH_4Cl, 0.5 M $NaH_2PO_2 \cdot H_2O$, and 0.05 M $FeCl_2 \cdot 4H_2O$;

(b) SEM image of a Sn film deposited at –0.65 V for 10 min. The inset figure is the EDX spectrum of the Sn film deposited at –0.65 V for 10 min.

(c) SEM image of the as-prepared $Fe_{51}Sn_{38}P_{11}$ electrode and elemental mapping images of (d) Fe, (e) Sn, and (f) P.

Figure 2 (a) Chemical composition of Fe-Sn-P alloy film prepared at various current densities; (b) XRD patterns of Fe-Sn-P alloys with different compositions.

Figure 3 EDX (a) and XPS spectra (b) of $Fe_{51}Sn_{38}P_{11}$ multiphase composite electrode.

Figure 4 Lithiation/delithiation capacities and coulombic efficiency of $Fe_{51}Sn_{38}P_{11}$, $Fe_{70}Sn_{16}P_{14}$, and $Fe_{73}Sn_{13}P_{14}$ (a–c) and (d) galvanostatic charge-discharge curves of $Fe_{51}Sn_{38}P_{11}$ multiphase composite electrode in the fixed voltage range of 1.5–0.02 V at a current density of 100 mA g^{-1}.

Figure 5 (a) SEM image of $Fe_{51}Sn_{38}P_{11}$ electrode after 90 cycles and elemental mapping images of (b) Fe, (c) Sn, and (d) P.

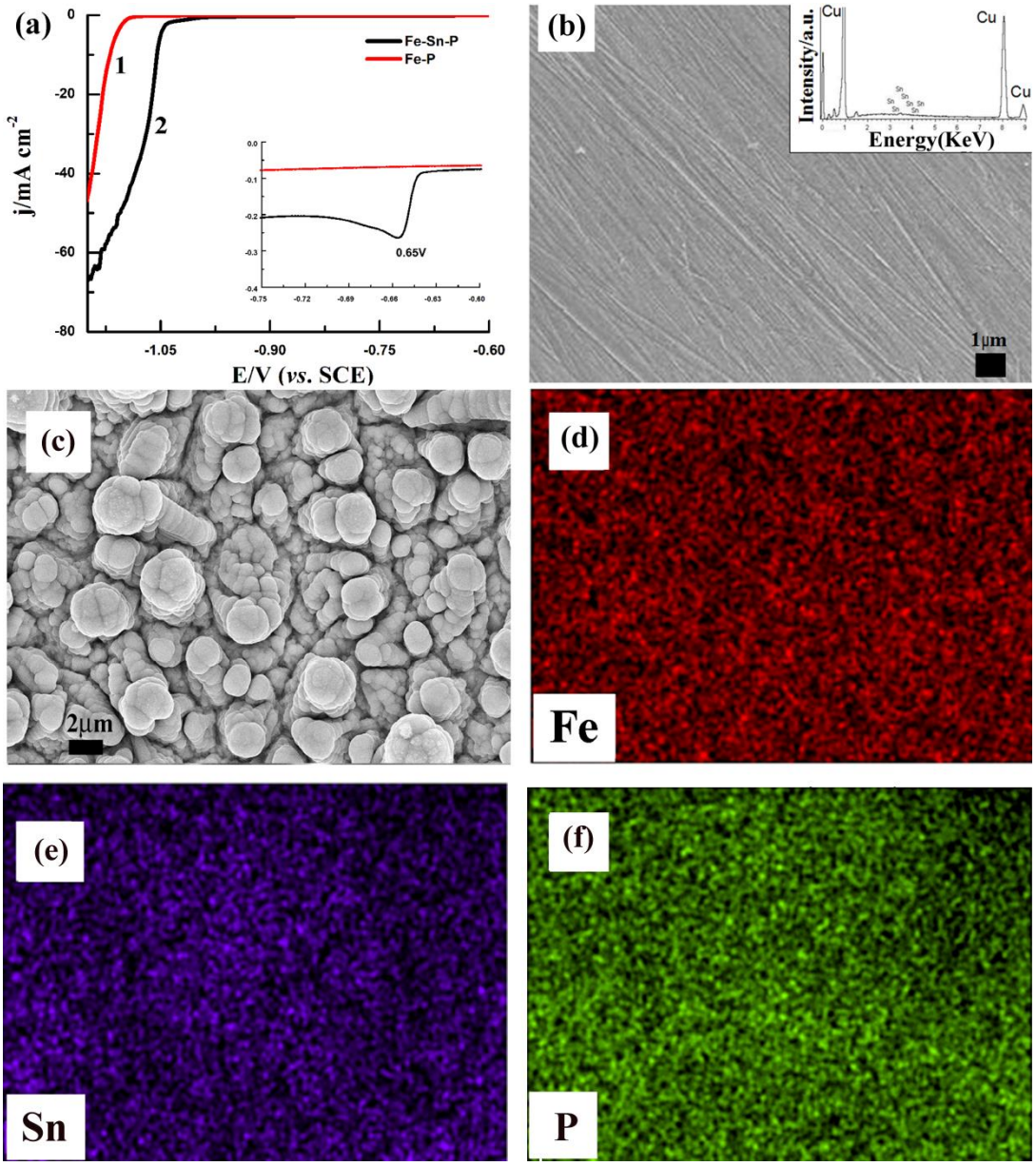
(a)
Fe-Sn-P
Fe-P
1
2
j/mA cm-2
E/V (vs. SCE)
0.65V
(b)
Cu
Cu
Cu
Intensity/a.u.
Energy(KeV)
1μm
(c)
2μm
(d)
Fe
(e)
Sn
(f)
P

Figure 1

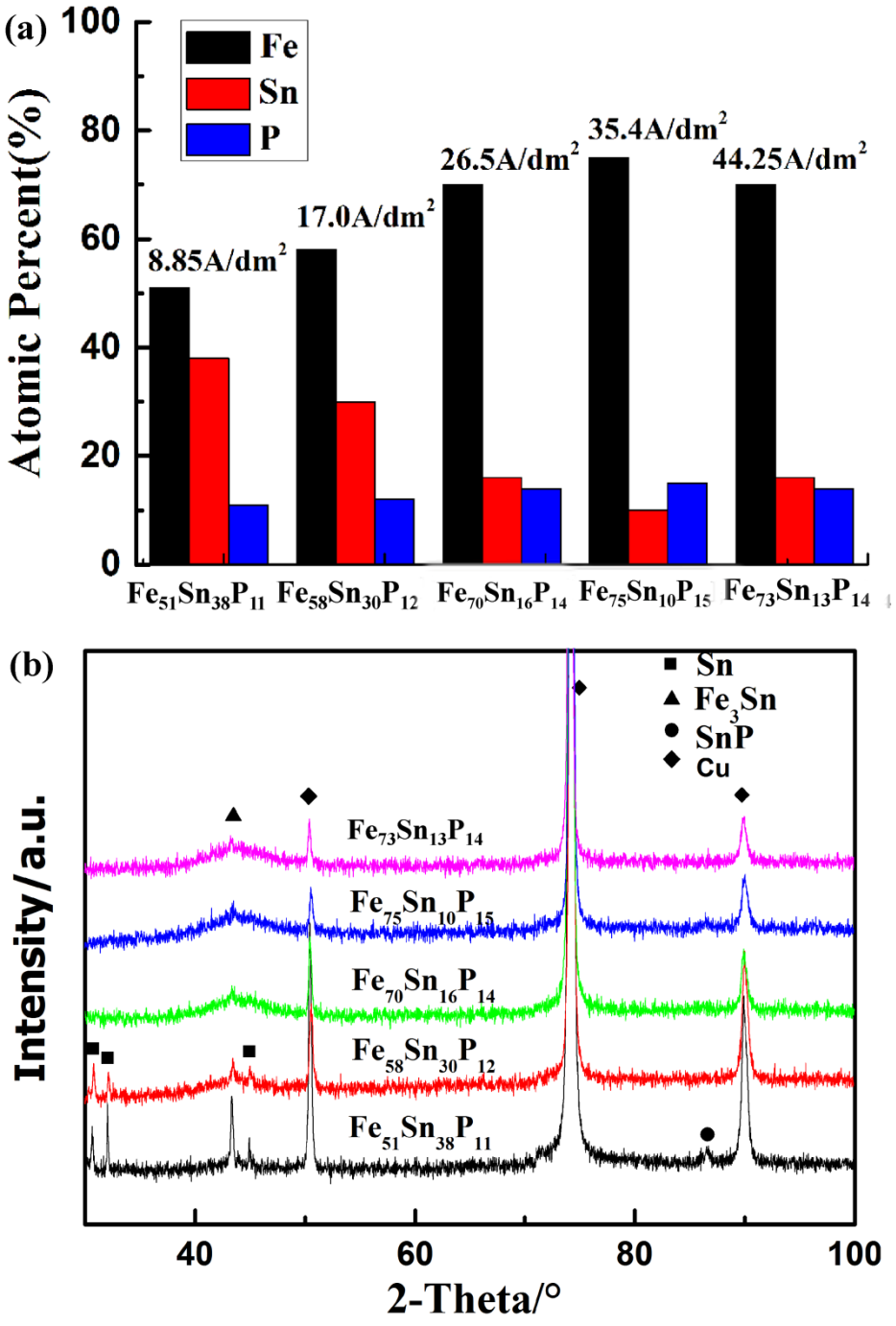
(a)
Atomic Percent(%)
Fe
Sn
P
8.85A/dm2
17.0A/dm2
26.5A/dm2
35.4A/dm2
44.25A/dm2
Fe51Sn38P11
Fe58Sn30P12
Fe70Sn16P14
Fe75Sn10P15
Fe73Sn13P14
(b)
Intensity/a.u.
Sn
Fe3Sn
SnP
Cu
Fe73Sn13P14
Fe75Sn10P15
Fe70Sn16P14
Fe58Sn30P12
Fe51Sn38P11
2-Theta/°

Figure 2

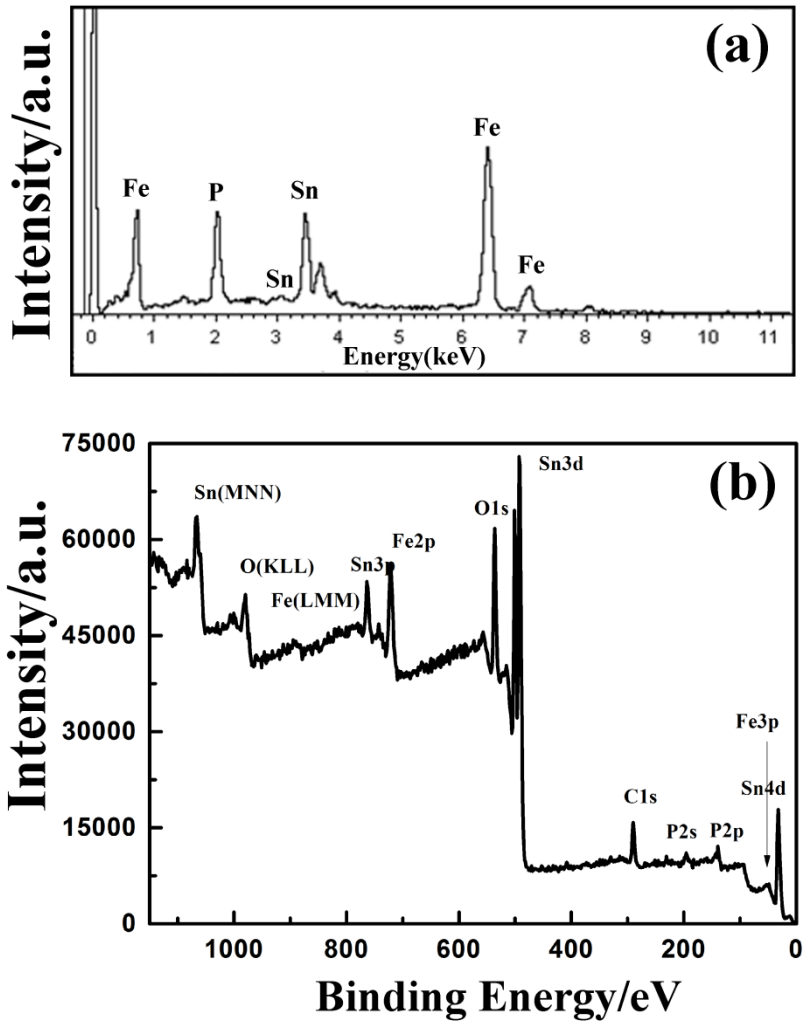
(a)
Intensity/a.u.
Fe
P
Sn
Sn
Fe
Fe
0
1
2
3
4
5
6
7
8
9
10
11
Energy(keV)
(b)
Intensity/a.u.
75000
60000
45000
30000
15000
0
Sn(MNN)
O(KLL)
Fe(LMM)
Sn3p
Fe2p
O1s
Sn3d
C1s
P2s
P2p
Fe3p
Sn4d
1000
800
600
400
200
0
Binding Energy/eV

Figure 3

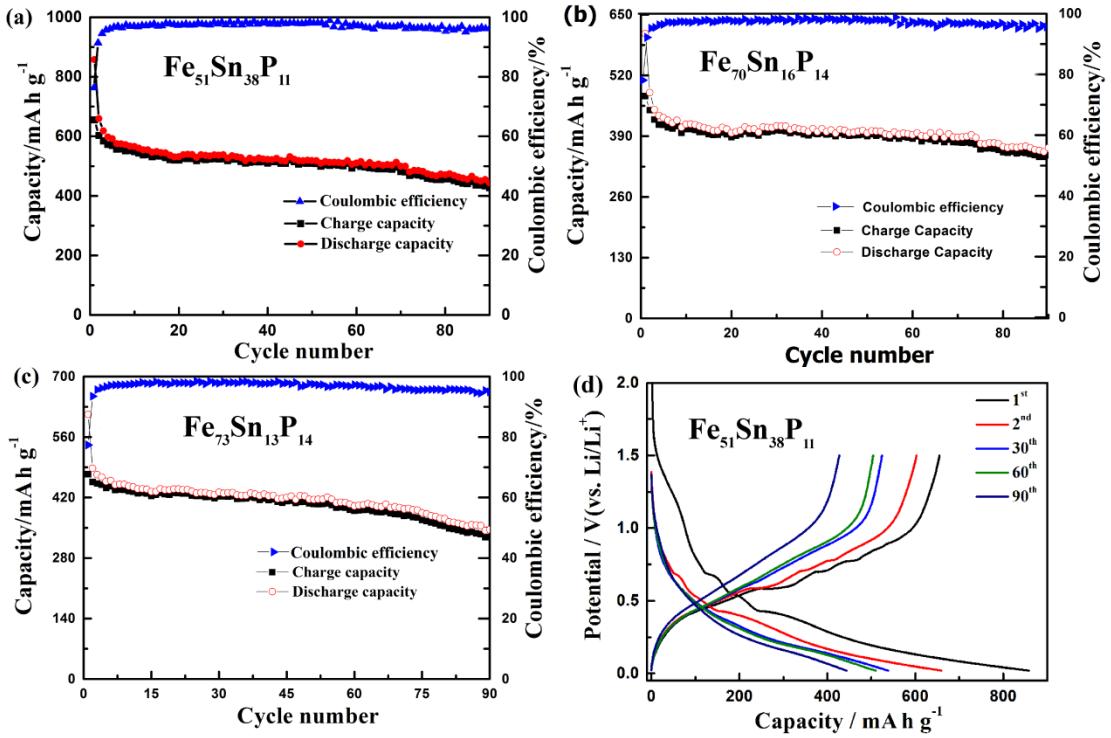
(a)
Fe51Sn38P11
Capacity/mA h g-1
Coulombic efficiency/%
Cycle number
Coulombic efficiency
Charge capacity
Discharge capacity
(b)
Fe70Sn16P14
Capacity/mA h g-1
Coulombic efficiency/%
Cycle number
Coulombic efficiency
Charge Capacity
Discharge Capacity
(c)
Fe73Sn13P14
Capacity/mA h g-1
Coulombic efficiency/%
Cycle number
Coulombic efficiency
Charge capacity
Discharge capacity
(d)
Fe51Sn38P11
Potential / V(vs. Li/Li+)
Capacity / mA h g-1
1st
2nd
30th
60th
90th

Figure 4

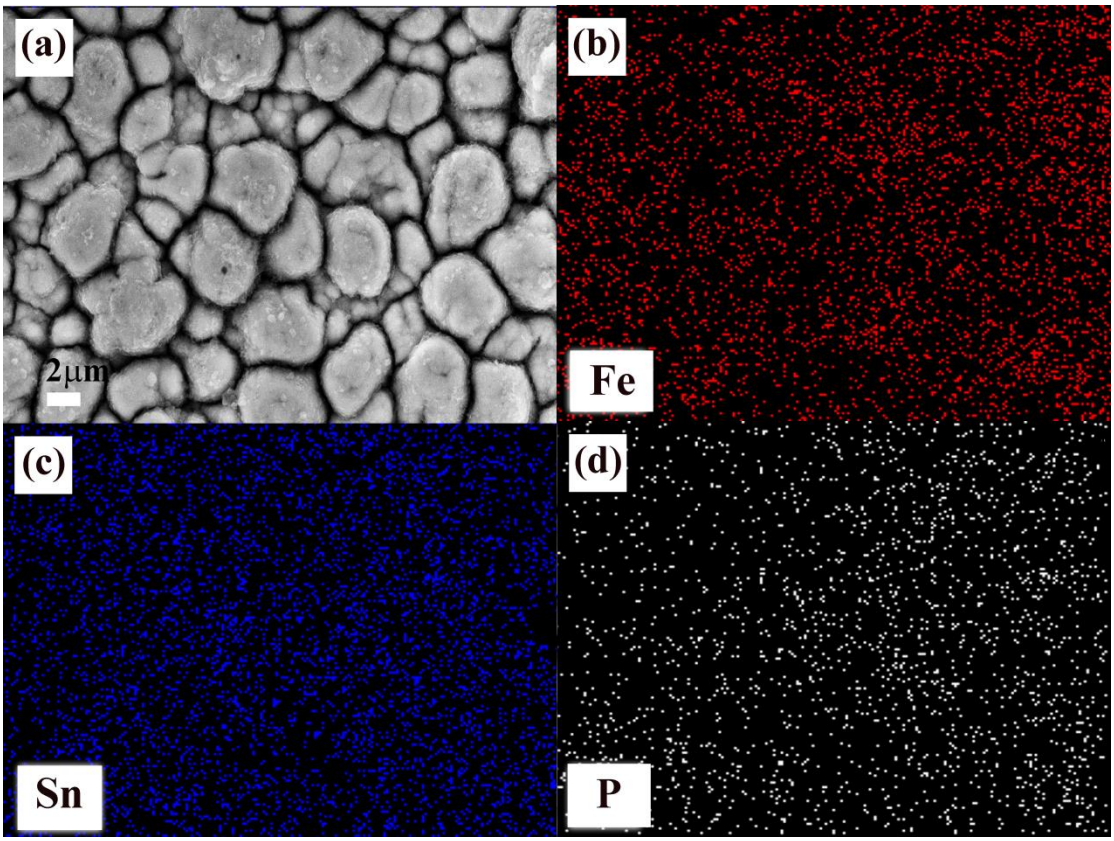

Figure 5